

# New constraints on the dust surrounding HR 4796 A

J. Milli<sup>1,2</sup>, D. Mawet<sup>2</sup>, C. Pinte<sup>3,1</sup>, A.-M. Lagrange<sup>1</sup>, D. Mouillet<sup>1</sup>, J. H. Girard<sup>2</sup>, J.-C. Augereau<sup>1</sup>, J. De Boer<sup>2</sup>, L. Pueyo<sup>4</sup>, and É. Choquet<sup>4</sup>

<sup>1</sup> Université Grenoble Alpes, IPAG, F-38000 Grenoble, France  
CNRS, IPAG, F-38000 Grenoble, France  
e-mail: julien.milli@obs.ujf-grenoble.fr

<sup>2</sup> European Southern Observatory (ESO), Alonso de Córdova 3107, Vitacura, Casilla 19001, Santiago, Chile

<sup>3</sup> UMI-FCA, CNRS/INSU France (UMI 3386), and Departamento de Astronomía, Universidad de Chile, Casilla 36-D Santiago, Chile

<sup>4</sup> Space Telescope Science Institute, 3700 San Martin Drive, Baltimore MD 21218, USA

Submitted to Astronomy & Astrophysics, March 31, 2014

## ABSTRACT

**Context.** HR 4796A is surrounded by a well-structured and very bright circumstellar disc shaped as an annulus with many interesting features: very sharp inner and outer edges, brightness asymmetries, center offset and suspected distortions in the ring.

**Aims.** We aim to constrain the properties of the dust surrounding the star HR 4796A, in particular the grain size and composition. We also want to confirm and refine the morphological parameters derived from previous scattered light observations, and reveal the dust spatial extent in regions unexplored so far due to their proximity to the star.

**Methods.** We have obtained new images in polarized light of the binary system HR 4796A and B in the Ks and L' band with the NaCo instrument at the Very Large Telescope (VLT). In addition, we revisit two archival data obtained in the L' band with that same instrument and at 2.2μm with the NICMOS instrument on the Hubble Space Telescope. We complement these observations with simulations using the radiative transfer code MCFOST to investigate the dust properties. We explore a grid of models with various dust composition and sizes.

**Results.** We detect the disc in polarized light in the Ks band and reveal for the first time the innermost regions down to 0.3'' along the minor axis. We measure a polarized fraction of  $29\% \pm 8\%$  in the two disc ansae, with a maximum occurring more than 13° westwards from the ansae. A very pronounced brightness asymmetry between the North-West and South-East side is detected. This contradicts the asymmetry previously reported in all images of the disc in unpolarized light at wavelengths smaller than or equal to 2.2μm and is inconsistent with the predicted scattered light from spherical grains using the Mie theory.

**Key words.** Instrumentation: high angular resolution - Stars: planetary systems - Stars: individual (HR 4796) - Instrumentation: Polarimeters - Scattering

## 1. Introduction

With a disc fractional luminosity of  $5 \times 10^{-3}$ , HR 4796 A is one of the brightest cold debris disc systems among main-sequence stars. It is an A0V star located at  $72.8 \pm 1.7$  pc. Together with HR 4796B, it forms a binary system with a projected separation of 560 AU. The dust was resolved at mid-infrared wavelengths (Koerner et al. 1998; Jayawardhana et al. 1998), at near-infrared wavelengths with NICMOS on the Hubble Space Telescope (HST) (Schneider et al. 1999) and from the ground, with adaptive optics (AO) (Mouillet et al. 1997; Augereau et al. 1999; Thalmann et al. 2011; Lagrange et al. 2012b; Wahhaj et al. 2014). It was also resolved at visible wavelengths with HST/ACS Schneider et al. (2009). The disc is confined to a narrow ring located at about 75 AU, seen with a position angle (PA) of 26.8° and inclined by 75.8° with respect to pole-on. In the optical, the East side (both North and South) was seen brighter than the West side with a 99.6% level of confidence (Schneider et al. 2009), which had led to the conclusion that the East side was inclined towards us with the common assumption of preferentially forward-scattering grains. Early modelling (Augereau et al. 1999) showed that two components are needed to explain the spectral energy distribution

(hereafter SED) up to 850μm and the resolved images up to thermal IR: a cold one, corresponding to the dust ring observed in scattered light, probably made of icy and porous amorphous silicate grains, plus a hotter one, with properties more similar to cometary grains, closer to the star. The need for the secondary component was debated by Li & Lunine (2003) but thermal images between 8 and 25μm with improved spatial resolution confirmed the presence of hot dust within  $\approx 10$  AU from the star (Wahhaj et al. 2005). More recent measurements of the far-infrared excess emission with APEX (Nilsson et al. 2010) and Herschel (Riviere-Marichalar et al. 2013) confirmed the presence of the cold dust component and could constrain its mass. The dust mass in grains below 1 mm was estimated to  $0.146 M_{\oplus}$  using the flux density at 870μm by Nilsson et al. (2010).

The high-angular resolution images of this system show that the disc ring is very narrow, with steep inner and outer edges, that were tentatively attributed to the truncation by unseen planets (Lagrange et al. 2012b). The morphology along the semi-minor axis of the disc, at about 0.3'', is poorly constrained, either because of the size of the coronagraph masking this inner region, as in Schneider et al. (2009) and Wahhaj et al. (2014), or because of the star-subtraction algorithm, i.e. angular differential imaging (ADI, Milli et al. 2012), that also removes much of the disc

flux at such a short separation as in Thalmann et al. (2011) and Lagrange et al. (2012b). Polarimetric differential imaging (hereafter PDI) is very efficient to suppress the stellar halo and reveal any scattered light down to  $0.1''$ . It is based on the fact that the direct light from the star is unpolarized while the light scattered by the dust grains of the disc shows a linear polarization. This technique was successfully used to characterize the protoplanetary discs around young stars (e.g. Mulders et al. 2013; Avenhaus et al. 2014). The first attempt to image the disc of HR 4796 using polarimetry was done by Hinkley et al. (2009) who obtained a  $6.5\sigma$  detection of the disc ansae at H band, using the 3.6m AEOS telescope and a lower limit on the polarization fraction of 29%. Modelling the scattered light images both in intensity and polarization is becoming a popular diagnostic tool for circumstellar discs because it brings constraints on the particles sizes and shapes (e.g. Min et al. 2012; Graham et al. 2007). It allows breaking the degeneracies coming from modelling the SED alone. On HR4796, Debes et al. (2008) proposed a population of dust grains dominated by  $1.4\mu\text{m}$  organic grains to explain the near-infrared dust reflectance spectra in intensity. In polarimetry, Hinkley et al. (2009) used simple morphological models, with an empirical scattering phase function and Rayleigh-like polarizability to conclude that their measurements are compatible with a micron-sized dust population. No attempts were made to use theoretical scattering phase function and to reconcile the SED-based modelling with the scattered light modelling. This will be discussed in this paper.

In section 2 and 3, we present a new set of resolved images of the HR 4796 debris disc : a new detection in Ks polarized light, a non-detection in  $L'$  polarized light, and two re-reductions of previously published images at those two wavelengths. The analysis of the morphology and the measured properties of the disc is made in section 4. An attempt to simultaneously fit the SED and scattered light images is presented in section 5 and discussed in section 6.

## 2. New polarimetric observations

### 2.1. Presentation of the data

The new observations are polarimetric measurements performed with VLT/NaCo in service mode in April and May 2013<sup>1</sup> (Rousset et al. 2003; Lenzen et al. 2003). Table 1 provides a log of the observations. The star was observed in field tracking, cube mode<sup>2</sup>, in the Ks ( $2.15\mu\text{m}$ ) and  $L'$  ( $3.8\mu\text{m}$ ) bands, with the S27 and L27 camera respectively, providing a plate scale of 27mas/pixel. The polarimetric mode of NaCo uses a Wollaston prism to split the incoming light into an ordinary and extraordinary beam,  $I_{ord}$  and  $I_{extra}$ , separated by  $3.30''$  and  $2.97''$  in the Ks and  $L'$  band respectively. A mask prevents the superimposition of the two beams but limits the field of view to stripes of  $27'' \times 3.3''$ . A rotative half-wave plate (HWP) located upstream in the optical path enables rotating the polarization plane. Polarization of light can be represented by means of the Stokes parameters (I,Q,U,V) (Stokes 1852), where I is the total intensity, Q and U are the linearly polarized intensities and V is the circularly polarized intensity. We did not consider circular polarization in this work because NaCo does not provide a quarter-wave plate to measure it. For each observation, we set the on-sky position angle to  $45.5^\circ$  in order to align the two components HR 4796A and HR 4796B along the polarimetric mask so that both stars

could be imaged on the same polarimetric stripe of the detector. We used two dither positions to allow for sky subtraction, the two components being either centered on the bottom left or bottom right quadrant of the detector. One full polarimetric cycle consisted in four orientations of the HWP:  $0^\circ$ ,  $45^\circ$  to measure Stokes Q, and  $22.5^\circ$ ,  $67.5^\circ$  to measure Stokes U. We acquired two integrations (DIT  $\times$  NDIT) with the same dither position per polarimetric cycle.

### 2.2. Data reduction

#### 2.2.1. Cosmetic and centering

All frames are sky-subtracted using the complementary dither positions and are then flat-field corrected. We noticed in the Ks band that the cosmetized collapsed cubes of image are still affected by two different kinds of electronic noise. One of them is described by Avenhaus et al. (2014) and affects some detector rows, it varies with a very short timescale within a data cube; it is therefore not corrected by a sky subtraction. We applied the row mean subtraction technique implemented by Avenhaus et al. (2014) in the H band to counteract this effect. The second source of noise affects only the bottom right quadrant of NaCo and leaves a predictable square pattern only visible after the polarimetric subtraction. We therefore ignored the frames where the star was located in that quadrant, because this solution turned out to surpass any other filtering algorithm that we tried. The relevant stripes of the polarimetric mask were then extracted. Star centering was done by fitting a Moffat profile on the unsaturated wings of the star (Lagrange et al. 2012a). We then performed a cross correlation between the ordinary and extraordinary images of the star to find the residual offset between those two frames and shifted the extraordinary image to the center of the ordinary image. The uncertainty on the star center is dominated by the fit of the saturated PSF by a Moffat function. To evaluate it, we followed the methodology described in Appendix A.1 from Lagrange et al. (2012a), using the unsaturated PSF from the binary companion HR 4796B and found an error of 8.7mas and 2.2mas in the horizontal and vertical direction of the detector respectively.

#### 2.2.2. Polarimetric subtraction

We briefly recall here the concepts of PDI in order to introduce the notation used hereafter. To derive the Stokes Q and U from the intensity measurements  $I_{ord}$  and  $I_{extra}$ , we performed the double ratio technique, following Tinbergen (2005). We also applied the double difference technique explained in detail in Canovas et al. (2011) but found in agreement with Avenhaus et al. (2014) that the former technique yielded a better signal-to-noise ratio (SNR). We computed the Q component of the degree of polarization,  $p_Q$ , using

$$p_Q = \frac{R_Q - 1}{R_Q + 1} \quad (1)$$

with

$$R_Q = \sqrt{\frac{I_{ord}^{0^\circ}/I_{extra}^{0^\circ}}{I_{ord}^{45^\circ}/I_{extra}^{45^\circ}}} \quad (2)$$

The Stokes Q parameter is then obtained with

$$Q = p_Q \times I_Q \quad (3)$$

<sup>1</sup> Based on observations made with ESO telescopes at the Paranal Observatory under Programme ID 091.C-0234(A)

<sup>2</sup> Individual frames are saved (Girard et al. 2010)

**Table 1.** Observing log

Date	UT start/end	Filter	DIT <sup>a</sup>	NDIT <sup>b</sup>	$N_{exp}$ <sup>c</sup>	$N_p$ <sup>d</sup>	$t_{exp}$ <sup>e</sup>	$\tau_0$ <sup>f</sup> (ms)	Seeing (")
17-04-2013	02:24/02:50	Ks	0.35	110	2	3	231	8	0.8
16-05-2013	03:03/04:07	Ks	0.5	100	2	8	800	6	1.4
15-05-2013	02:49/03:56	L'	0.2	120	2	10	480	3	0.6

**Notes.** <sup>(a)</sup> Detector Integration Time in seconds. <sup>(b)</sup> Number of DIT. <sup>(c)</sup> Number of exposures per polarimetric cycle. <sup>(d)</sup> Number of polarimetric cycles. <sup>(e)</sup> Total exposure time per HWP position in seconds. <sup>(f)</sup> Coherence time as indicated in the frame headers.

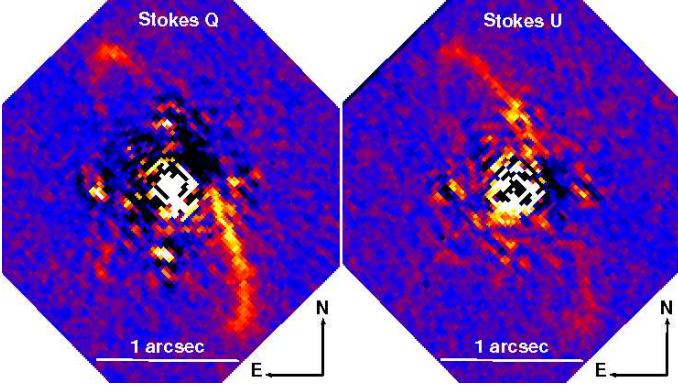


**Fig. 1.** Stokes Q and U images in the Ks band before correcting for the instrumental polarization.

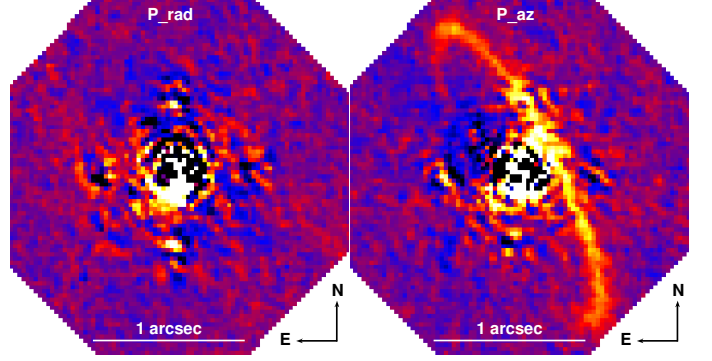


**Fig. 2.** Radial and tangential Stokes after correcting for the instrumental polarization.

where  $I_Q$  stands for the mean intensity in the images used with the HWP in position  $0^\circ$  and  $45^\circ$ :

$$I_Q = 0.5 \times (I_{ord}^{0^\circ} + I_{extra}^{0^\circ} + I_{ord}^{45^\circ} + I_{extra}^{45^\circ}) \quad (4)$$

Replacing the upperscripts  $0^\circ$  and  $45^\circ$  by  $22.5^\circ$  and  $67.5^\circ$  gives the equations used to derive the Stokes U image. Both Stokes images are shown in Fig. 1. The tangential and radial Stokes parameters are then derived using:

$$P_{\parallel} = Q \cos(2\phi) + U \sin(2\phi) \quad (5)$$

$$P_{\perp} = -Q \sin(2\phi) + U \cos(2\phi) \quad (6)$$

where  $\phi$  is defined as the angle between the vertical on the detector and the line passing through the star located at  $(x_0, y_0)$  and the position of interest  $(x, y)$ :

$$\phi = \arctan\left(\frac{x - x_0}{y - y_0}\right) + \theta \quad (7)$$

The offset  $\theta$  accounts for a slight misalignment of the HWP. It was estimated from the data, as explained in the next section.

### 2.2.3. Correction for instrumental polarization

Because it stands at the Nasmyth focus of the VLT after the  $45^\circ$  tilted mirror M3 and also has many inclined surfaces, NaCo suffers from significant instrumental polarisation effects (Witzel et al. 2011). To achieve the best polarimetric sensitivity and accuracy, we must correct for it. Although HR 4796A is saturated, we can use the unsaturated companion star to renormalize the images. We made the assumption that HR 4796B is not polarized and imposed that its flux in the ordinary and extraordinary image is equal. To do so, we renormalized the ordinary / extraordinary image by the integrated flux of HR 4796 B in the ordinary / extraordinary image. We checked that the scaling factor was consistent with the value derived using the unsaturated

halo of the star HR4796A, as done by Avenhaus et al. (2014). Both values agree within 1%. Further instrumental polarization remains, in particular we noticed that the disc flux in Stokes Q is unexpectedly higher than in Stokes U (Fig. 1). This effect represents a loss in polarimetric efficiency and is distinct to the former additive instrumental polarization described above. It was also detected by Avenhaus et al. (2014) when observing HD 142527, and it is probably due to crosstalks between the U and V components of the Stokes vectors and to the lower throughput for Stokes U within NAOS (see the NAOS Mueller matrix displayed in Eq. 16 of Witzel et al. 2011). They corrected for this effect by assuming that there must be as many disc pixels with  $|Q| \geq |U|$  as with  $|U| \geq |Q|$  and derived the Stokes U efficiency  $e_U$  that satisfied this condition. While this assumption holds true for a pole-on disc like HD 142527, this is not necessarily true for an inclined disc such as HR 4796, depending on its position angle on the detector. Instead, we assumed that the grain population is homogenous between the South-East (SE) and North-West (NW) ansae, therefore the polarization fraction must be the same. Because the Stokes Q and U contribute differently to the polarized flux of each ansae, we could find a value for  $e_U$  that yields the same polarization fraction in both ansae averaged for the scattering angles between  $88^\circ$  and  $90^\circ$ . We derived  $e_U = 76\%$ . This value is within the typical Stokes U efficiencies derived in the past with NaCo (from 55.0% to 77.8%, Avenhaus et al. 2014). We also corrected for a possible misalignment of the HWP or a cross-talk between the Stokes Q and U. To do so, we introduced the offset  $\theta$  in Eq. 7. For an optically thin disc, we do not expect any signal in the radial Stokes  $P_{\perp}$ , it must therefore be 0 in the absence of noise. A value  $\theta = -5.4^\circ$  was found to validate this property on average in the elliptical disc region, in agreement with the typical values measured with NaCo (between  $-3.7^\circ$  and  $-7.0^\circ$ , Avenhaus et al. 2014). The radial and tangential Stokes parameters after correcting for the instrumental polarization are shown in Fig. 2. Most of the structures disappear in the radial polarization.



### 2.3. Subtraction of the point-spread function in intensity images

In addition to the polarized intensity, the total intensity (Stokes I) contained in the sum  $I_{ord} + I_{extra}$  is also a valuable information to characterize light scattered by circumstellar matter. This sum contains the contribution of the star and the disc, it is therefore necessary to remove the contribution of the star to obtain the intensity of the disc. We used the binary component HR 4796 B to build a library of reference point spread functions (PSF), that we later used to estimate the PSF to subtract from the intensity images of HR 4796 A. To do so, we used the Principal Component Analysis (hereafter PCA) technique described in Soummer et al. (2012). Because HR 4796B is located at a projected separation of  $7.7''$  where the distortion and variation in AO correction remains limited, and because it can be imaged simultaneously, this library represents a representative set of reference PSF.

### 2.4. Detection limits

#### 2.4.1. Disc detection in the Ks band for the Stokes Q and U

In the Ks band, we detect the disc in the Stokes Q and U images of both the April and May 2013 observations, but not in the Stokes I image. The May observations have a much higher integration time, and we did not find any improvement in combining both epochs. We therefore only present and analyse the images of this data set (Fig. 1, 2 and 3, left). The disc is detected with a SNR of 9 in the ansae  $1''$  away from the star (respectively  $\sim 5$ ,  $\sim 3$  for the Stokes Q and U image, the Stokes U image having an increased noise level). The disc is detected down to  $0.25''$  on the North-West (NW) side where it appears the brightest. The square pattern observed with a size of  $0.76''$  is the waffle mode of NaCo and corresponds to a spatial frequency of  $7\lambda/d$ .

We used the unsaturated binary companion HR 4796 B measured simultaneously to flux-calibrate our data. Using a K magnitude of 8.35 for the companion star, we are sensitive, in polarized light, to extended emission  $2.5\text{mag/arcsec}^2$  fainter than the star at a separation of  $0.1''$  and  $8\text{mag/arcsec}^2$   $1''$  away from the star, as shown in Fig. 4. We also overplotted the detected flux of the disc in polarized intensity. In total intensity, our contrast is degraded by 4 magnitudes (black dotted curve). Despite using one of the most advanced PSF subtraction algorithms (PCA), we clearly cannot detect the disc in intensity given this level of contrast. Visual tests show that injecting a synthetic disc about 10 times brighter than the real disc leads to a  $> 5\sigma$  detection in the ansae.

#### 2.4.2. Non detection in the L' band

The disc is not detected in the L' band neither in polarimetry (Stokes Q or U) nor in intensity (Stokes I) with the current data set. The contrast level reached in the polarized intensity image is shown in Fig. 4 (red curve). Unlike in the Ks band, the contrast curve is flat beyond  $2''$ , indicating that we are not limited by the residual light from the star. As the data reduction procedure was done in the exact same way as in the Ks band, this poor result comes from the shorter total integration time and the specificity of the L' band regarding the thermal emission and the optics transmission. The observational strategy implied a change in the dither position every 7min which happened to be too slow in the L' band where the background is significantly higher and more variable than in the Ks band. Moreover, the Wollaston transmis-

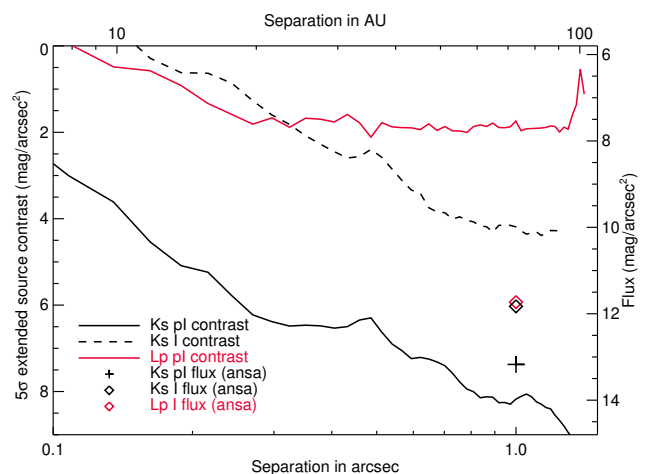


**Fig. 4.** Contrast level reached in intensity (dotted curve) and polarized intensity (plain curves) for the Ks data (in black) and for the L' data (in red). The mean flux density in the ansae as measured with NaCo (black cross and red diamond) and NICMOS (black diamond) are overplotted.

sion drops to about 85% due to an MgFe cristal absorption band at  $3.4\mu\text{m}$ .

From our photometry of the disc in L' (red diamond in Fig. 4, see section 4.2.2 for details on the derivation), we conclude that our current polarization detection limits are more than one magnitude above the disc flux density in the ansae. Therefore even if 100% of the scattered light were polarized, we would still not detect it.

## 3. Analysis of archival data at $2.2\mu\text{m}$ and in the L' band

### 3.1. HST/NICMOS at $2.2\mu\text{m}$

Because the disc is not detected in Stokes I in our new polarimetric data, we used archival data of HR 4796 from HST NICMOS in the F222M filter (central wavelength at  $2.22\mu\text{m}$ ). The star was observed at two roll angles on August, 12 2009 (Proposal id: 10167, PI: A. Weinberger) for a total integration time of 36min. We reprocessed the data using the reference star subtraction technique based on PCA with a library of NICMOS PSF (Soummer et al. 2014). The newly reduced image is shown in Fig. 3 (middle).

### 3.2. VLT/NaCo in the L' band

We revisited previous observations of the disc in the L' from Lagrange et al. (2012b) for three reasons:

1. to check whether our non-detection in polarization is compatible with the existing detection of the disc in this band in intensity. In Lagrange et al. (2012b) we did not measure the photometry of the disc.
2. to get additional constraints on the dust colour.
3. to compare the morphological parameters of the disc using the same measurement method

Since the release of the paper in 2012, more efficient reduction algorithms to reveal faint extended emission from circumstellar discs were developed, e.g. PCA (Soummer et al. 2012). We re-reduced the data using this technique. The final image is shown in Fig. 3 (right), and has an increased SNR.

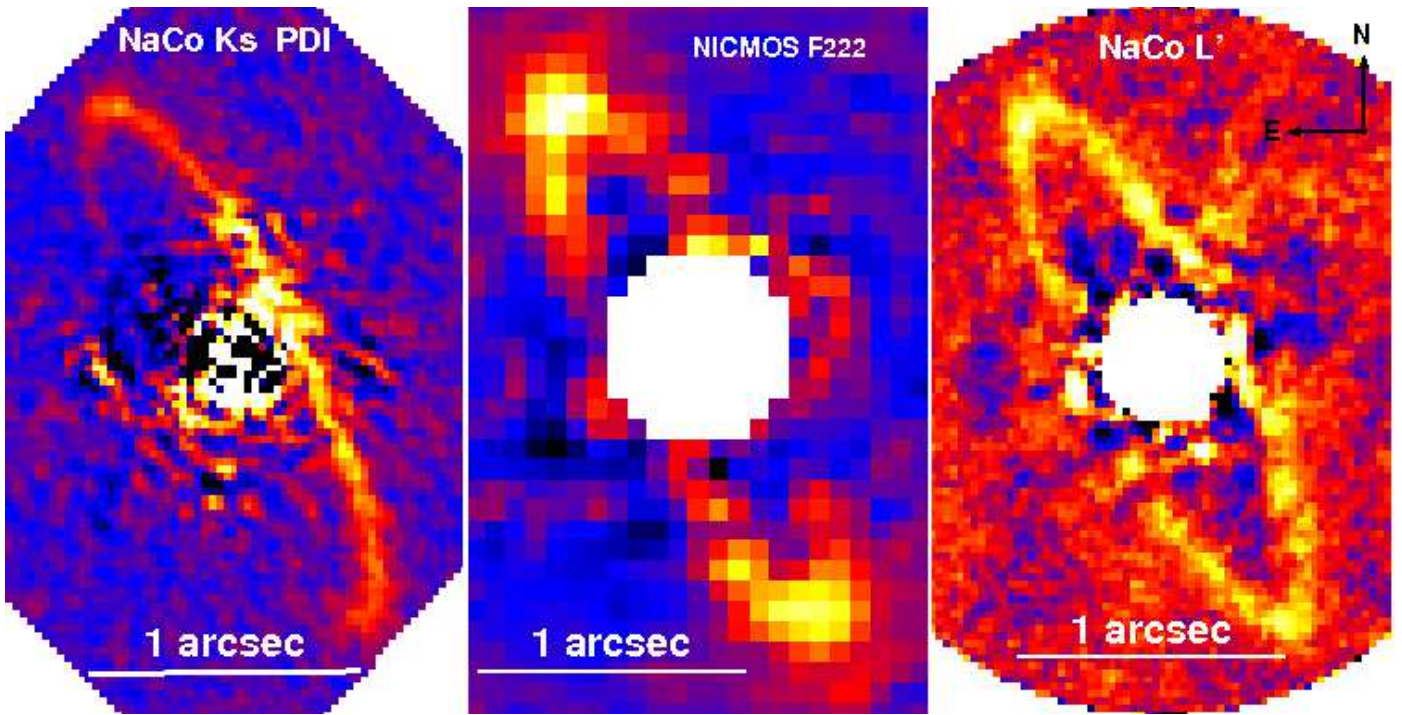


**Fig. 3.** Left: Ks polarized intensity image of the disc. Middle: NICMOS image at  $2.2\mu\text{m}$  (new reduction). Right: NaCo  $L'$  image (new reduction). The colorscale is linear.

## 4. Analysis

### 4.1. Brightness asymmetries

The most puzzling feature revealed by our new polarimetric observations is a very significant brightness asymmetry with respect to the semi-major axis of the star, with the North-West (NW) side much brighter than the South-East (SE) side (Fig. 3 left). We note that the first light images of the Gemini Planet Imager (GPI) on HR 4796 A also detects this asymmetry (Perrin et al., submitted). The polarized flux reaches  $3.4\text{mJy/arcsec}^2 \pm 0.4$  in the NE ansa whereas the SE side of the disc is not detected in polarimetry, its flux being below the noise level within  $0.7''$ . This new asymmetry contrasts with the NICMOS image (Fig. 3 middle) showing the opposite trend, and with all previous scattered light observations below  $3\mu\text{m}$  (Debes et al. 2008). From these previous observations and assuming that dust is generally preferentially forward-scattering, it was assumed that the SE side was the side inclined towards the Earth (Schneider et al. 2009). To be consistent with our modelling presented in section 5, we will here use the opposite assumption as our baseline scenario: the NW side is the side inclined towards the Earth. Under this assumption, Fig. 5 summarizes the anisotropic behaviour of the dust reported in intensity images in the optical and near-infrared. The anisotropy of scattering is generally described by the empirical Henyey-Greenstein phase function, which is parametrized by a single coefficient called  $g$ . A negative value of  $g$  indicates in our baseline scenario that the SE side is brighter than the NW side. Although there is a jump after  $1.6\mu\text{m}$ , the overall trends seems to indicate that the dust becomes more and more isotropic at longer near-infrared wavelengths. This trend is confirmed by our new reduction at  $L'$  (Fig. 3 right), where the NW side is seen slightly brighter than the SE side at  $2.1\sigma$ . This intriguing behavior will be discussed in the section 5.5.3.

A second brightness asymmetry was reported in the past with respect to the NE and SW ansae. This asymmetry is thought to be

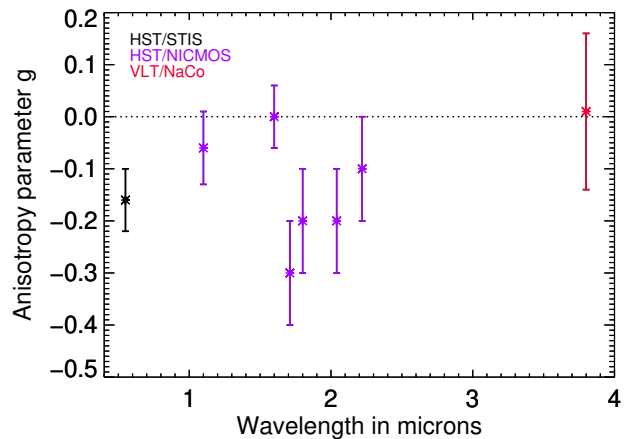


**Fig. 5.** Evolution of the Henyey-Greenstein  $g$  coefficient with wavelength. It is based on the values derived by Debes et al. (2008) and Schneider et al. (2009) for the HST images, using scattering angles between  $5^\circ$  and  $15^\circ$  from the major axis, and on our results for the VLT/NaCo new reduction at  $L'$  (section 4.2.2).

partially caused by pericenter glow due to the offset of the disc (Schneider et al. 2009; Moerchen et al. 2011), but this explanation is not sufficient to account for the amplitude the asymmetry (Wahhaj et al. 2014). Our new polarization image also shows this asymmetry with a ratio between the NE and SW ansae of  $1.07 \pm 0.15$ . In the unpolarized NICMOS image, this ratio is slightly less  $1.04 \pm 0.36$  but it reaches  $1.34 \pm 0.23$  in the  $L'$  image.

## 4.2. Ring geometry

### 4.2.1. Constraints from polarized observations

We note a small distortion in the SW at a separation of  $0.4''$  and a position angle of  $235^\circ$ . Such a feature is also present at the same position in H band and optical images (Thalmann et al. 2011), and in our  $L'$  image (Fig. 3 right, already detected in the initial reduction by Lagrange et al. 2012b).

To compare the morphology of the disc in polarized light with previous measurements, we interpreted the disc as an inclined circular ring and measured its center position with respect to the star, its radius, its inclination and its position angle (PA). We built a scattered light model of the disc in intensity using the GRaTeR<sup>3</sup> code Augereau et al. (1999) with the same parametrization as presented in Lagrange et al. (2012b). The model geometry is defined by six free parameters: the center offset along the semi-major axis ( $x_c$ ) and semi-minor axis ( $y_c$ ), the inclination  $i$ , the PA, the radius  $r_0$  and a scaling factor to match the disc total flux. We modelled the SE to NW asymmetry by a smooth function peaked on the NW side along the semi-minor axis and canceling  $30^\circ$  away from the ansa westwards. Our aim, here, is not to constrain the dust properties by modelling the scattering phase function but only to build a map of the disc that is consistent with the disc morphology. Constraining the grain properties will be the focus of the section 6.

We then minimized a chi squared  $\chi^2$  between our synthetic image and our model. The results are shown in Table 2 (first row). The offset of the disc evaluated by Schneider et al. (2009) in the optical to  $x_c = 1.4 \pm 0.4$  AU and by Wahhaj et al. (2014) to  $x_c = 1.2 \pm 0.1$  AU is also detected in our data with a larger uncertainty:  $x_c = 0.8^{+3.5}_{-3.0}$  AU. This uncertainty, given at  $3\sigma$ , includes the error on the star center but this contribution is not dominant because these observations are done without coronagraph, unlike the HST/STIS observations.

### 4.2.2. Constraints from $L'$ unpolarized observations

To measure the morphology of the disc in the  $L'$ , we kept the same parametric model as described previously and added the possibility to model anisotropy of scattering with a Henyey-Greenstein phase function. In that case, the Henyey-Greenstein g coefficient is an additional free parameter. Because the star subtraction is performed using ADI, the disc can be significantly self-subtracted (Milli et al. 2012), and we implemented the forward-modelling technique already described in Milli et al. (2014) for  $\beta$  Pictoris in order to retrieve the best disc parameters. The results are shown in Table 2. Our results agree with the values already published in Lagrange et al. (2012b). They are compatible with a disc scattering light isotropically. The offset detected along the semi-minor axis explains the NW/SE asymmetry without the need for anisotropic scattering. An offset of  $y_c = -1.15 \pm 0.16$  AU along the semi-minor axis was already detected by Thalmann et al. (2011) in the H band.

## 4.3. Photometry in the Ks band

### 4.3.1. Polarized light

In polarized light, we find a polarized flux of  $13.2 \text{ mag/arcsec}^2 \pm 0.1$  and  $12.3 \text{ mag/arcsec}^2 \pm 0.1$  for the NE and SW ansae of the disc, at a projected separation of  $1.05''$  or  $76.7 \text{ AU}$ . The uncer-

<sup>3</sup> GRaTeR is very fast and optimized for optically thin debris discs, it is therefore more adapted to forward modelling than MCFOST.

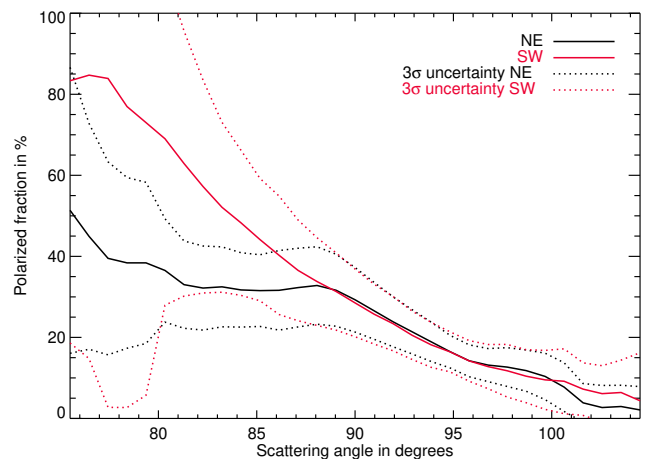


**Fig. 6.** Polarized fraction as a function of the scattering phase angle, measured from NaCo Ks polarized intensity and NICMOS intensity. A phase angle of  $0^\circ$  indicates the NW side and  $90^\circ$  corresponds either to the NE or SW ansa.

tainty is computed as three times the azimuthal root mean square in the radial Stokes and does not take into account systematic errors that could arise from a bad calibrations of the instrumental polarization. The polarized flux is maximal along the semi-minor axis, on the North-West (NW) side.

### 4.3.2. Unpolarized light

Below  $0.6''$ , the noise dominates the image, so we restricted the photometry of the disc to an elliptical aperture beyond  $0.6''$  as done by Debes et al. (2008). We used an isotropic model of the disc to correct for the flux loss due to PCA and for the disc flux not measured in the aperture. We find a total disc flux of  $3.7 \pm 0.26 \text{ mJy}$  compatible with the  $3.5 \pm 0.2 \text{ mJy}$  measured by Debes et al. (2008).

## 4.4. Polarized fraction

The polarized fraction (Fig. 6) was computed as the ratio of the NaCo pI image over the NICMOS I image. It can only be computed reliably within  $15^\circ$  of the ansae due to the residual noise affecting the NICMOS image beyond this range. It reaches  $29.3\% \pm 8.0\%$  and  $28.5\% \pm 8.4\%$  in the NE and SW ansae. It is increasing continuously westwards from both ansae for at least  $15^\circ$ . If we assume that the side inclined towards us is the NW side (see discussion in section 6), then it means that the peak polarization fraction occurs below a scattering angle of  $90^\circ$  and we can state that the polarized fraction is above 22% for scattering angles between  $80^\circ$  and  $90^\circ$  with a 99.7% confidence level. Although the polarized fraction is very similar on both sides of the disc above a scattering angle of  $90^\circ$ , stronger values are measured below  $88^\circ$  for the SW side. However our large error bars are still compatible with a similar behavior for the dust on both sides.

## 4.5. Disc colour

From our measurements at two different wavelengths, we calculated a colour index defined as  $\frac{I_{\text{disc},L'}}{I_{\text{disc},Ks}} / \frac{I_{\star,L'}}{I_{\star,Ks}}$  where  $I_{\text{disc}}$  is the disc flux density and  $I_{\star}$  is the star flux density at the specified wavelength, both measured in the ansae for the reason explained pre-



**Table 2.** Measurements of the morphology of the disc from the Ks polarized intensity image and Lp intensity image.  $x_c$  is the offset along the major-axis (negative means the SW side is closer to the star).  $y_c$  is the deprojected offset along the minor-axis (negative means the NW side is closer to the star). The uncertainty is given at  $3\sigma$  and includes the uncertainty from the measurement and the star position. In L' we investigated two scenarios: an isotropic disc and an anisotropic disc.

Filter	Polarization	PA	$r_0$ (AU)	$i$	$x_c$ (AU)	$y_c$ (AU)	$g$	$\chi^2$
Ks	Yes	$26.7^{+1.6}_{-2.2}$	$75.3^{+2.0}_{-2.2}$	$75.5^{+1.3}_{-1.7}$	$0.8^{+3.5}_{-3.0}$	$-5.8^{+8.3}_{-9.6}$	NA	1.6
L'	No	$26.9^{+1.5}_{-1.2}$	$74.9^{+2.1}_{-1.8}$	$76.0^{+1.5}_{-1.8}$	$1.9^{+3.0}_{-3.0}$	$-3.5^{+9.6}_{-9.9}$	0 <sup>a</sup>	0.93
L'	No	$26.9^{+1.5}_{-1.2}$	$74.8^{+2.1}_{-1.8}$	$75.8^{+1.5}_{-1.8}$	$2.0^{+3.0}_{-3.0}$	$-3.5^{+9.3}_{-9.9}$	$0.01^{+0.15}_{-0.18}$	0.93

**Notes.** <sup>(a)</sup> Fixed parameter.

viously. We find a value of  $1.1 \pm 0.6$ . Although the error bar is relatively large, this extends the conclusion by Debes et al. (2008) of a dust spectral reflectance flattening beyond  $1.6\mu\text{m}$ . Their conclusion was based and valid only up to  $2.2\mu\text{m}$ , we provide here a new photometric point at L' and measure that the flattening is valid until  $3.8\mu\text{m}$ .

## 5. Modelling

In the previous section, we revealed a very puzzling brightness inversion between the NW and SE sides of the disc and presented new observational constraints. To test these features against our current understanding of light scattering by dust particles, we modeled the radiative transfer in the disc and generated synthetic scattered light images.

Contrary to what was assumed before (Schneider et al. 2009), our baseline scenario to explain these features and which is discussed in this section, is the following: the NW side of the ring is inclined towards the Earth.

### 5.1. Approach and assumptions

Within the scope of this paper, we investigate whether a disc model can simultaneously fit the SED and explain the scattered light images. Extensive modelling work of the SED of the disc around HR 4796 has already been performed in past studies (e.g. Augereau et al. 1999; Li & Lunine 2003) to constrain the dust geometrical extension and properties. SED modelling is the most constraining approach, therefore, we do not explore a systematic grid of models and we limit our exploration to a parameter space that has already been shown to be compatible with the SED. We chose here to start from the previous modelling work made by Augereau et al. (1999) that could already explain the SED, as well as some resolved scattered light and thermal observations, and explored the parameter space around their best-fit model. Our new observations can constrain the cold outer dust component of their model that is responsible for the far infrared excess beyond  $25\mu\text{m}$ . The best model able to reproduce the far infrared emission (model #13) assumes a population of dust grain with sizes between  $a_{\min} = 10\mu\text{m}$  to  $a_{\max} = 1.4\text{m}$  with a  $s = -3.5$  exponential decay, and composed of porous silicates coated by an organic refractory mantle with water ice partially filling the holes due to porosity. We keep the same notation as in their paper, namely a total porosity  $P_{\text{wH}_2\text{O}}$ , a fraction of vacuum removed by the ice  $p_{\text{H}_2\text{O}}$ , a silicates over organic refractory volume fraction  $q_{\text{Sior}}$ . The porosity of the grain once the ice has been removed is written  $P$ . Model #13 of Augereau et al. (1999) used a porosity  $P$  of 59.8% and  $p_{\text{H}_2\text{O}} = 3\%$ . We reproduced their model with the radiative transfer code MCFOST (Pinte et al. 2006, 2009), we used the effective medium theory (EMT) to derive the optical indices of the grains, and we used the Mie theory (Mie 1908)

to compute their absorption and scattering properties. The EMT-Mie theory assumes porous spheres, which is probably not realistic for fluffy aggregates larger than  $1\mu\text{m}$  and can lead to unrealistic scattering properties (Voshchinnikov et al. 2007). We therefore also investigated a statistical approach, known as the distribution of hollow spheres (DHS, Min et al. 2005). This approach averages the optical properties of hollow spheres over the fraction of the central vacuum and was proven successful to reproduce the scattered light behaviour of randomly oriented irregular quartz particles. In both cases (Mie and DHS), we use the full scattering matrix to compute the synthetic intensity and polarisation maps. This is a major difference with Augereau et al. (1999) who adopted the empirical Henyey-Greenstein phase function. This choice was purposely made because an incompatibility between the SED and the scattered light images predicted by the Mie theory was already seen at the time. The Mie phase function for large grains predicted by the SED modelling exhibits indeed a very pronounced peak for small scattering angles.

Starting over from this initial model, we explored around this solution a reasonably exhaustive grid of 768 models in the parameter space ( $a_{\min}$ ,  $P$ ,  $p_{\text{H}_2\text{O}}$ ,  $q_{\text{Sior}}$ ,  $s$ ). The details of the grid are summarized in Table 3. Unlike Augereau et al. (1999), the only fitted value is the total dust mass that is scaled in order to minimize a  $\chi^2$  between the synthetic SED and eight SED measurements above  $20\mu\text{m}$  (listed in Table 4). This approach is correct if the disc is optically thin along the line of sight. We validated this assumption by re-running the simulation for the best models with the corrected dust mass. We assumed a population of dust grains located in an annulus centered about the star, whose radial volume density in the midplane follows a piecewise exponential law of index 9.25 before  $R_c = 74.2\text{AU}$  and -12.5 after this radius. For the vertical distribution, we assumed a gaussian profile of scale height  $H = 1\text{AU}$  at  $R_c$ . This represents a slight revision with respect to Augereau et al. (1999) who used a wider vertical profile less compatible with the new observations. The aspect ratio  $H/R_c$  is here 0.013, similar to Fomalhaut and slightly lower than the "natural" aspect ratio of  $0.04 \pm 0.2$  derived by Thébaud (2009) for debris discs.

### 5.2. Fit of the SED

We show the six best models with respect to the SED in Table 5. The best fit gives a reduced  $\chi^2$  of 3.0 and is shown in Fig. 7. We confirm that the SED modelling points towards large grains with minimum sizes above  $1\mu\text{m}$ : among the 20 models best fitting the SED all have a minimum grain size of 5 or  $10\mu\text{m}$ . We found an improvement by using a slightly higher carbon content

<sup>4</sup> This approach is consistent with the findings of Augereau et al. (1999) who showed that the cold annulus seen in scattered light contributes to 90% of the measured excess at  $20.8\mu\text{m}$

**Table 4.** Infrared and submillimeter flux density used in the SED fitting procedure. These measurement are posterior to the ones used in the early modelling by Augereau et al. (1999)

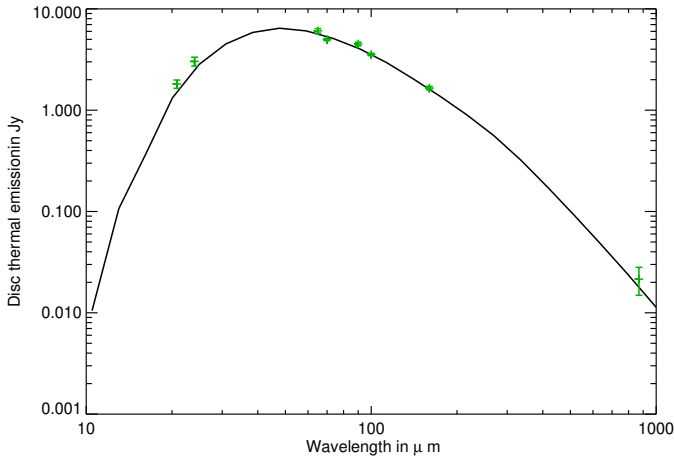
$\lambda$ ( $\mu\text{m}$ )	Flux density (Jy)	Error (Jy)	Instrument	Source
20.8	1.813	0.17	MIRLIN	Koerner et al. (1998)
24	3.03	0.303	SPITZER MIPS	Low et al. (2005)
65	6.071	0.313	AKARI	Yamamura et al. (2010)
70	4.98	0.131	HERSCHEL PACS	Riviere-Marichalar et al. (2013)
90	4.501	0.186	AKARI	Yamamura et al. (2010)
100	3.553	0.097	HERSCHEL PACS	Riviere-Marichalar et al. (2013)
160	1.653	0.068	HERSCHEL PACS	Riviere-Marichalar et al. (2013)
870	0.0215	0.0066	LABOCA APEX	Nilsson et al. (2010)

**Table 3.** Initial grid of parameters, amounting to a total of 768 models

Parameter	Values explored
Scattering theory	[Mie;DHS]
$a_{min}$ ( $\mu\text{m}$ )	[0.1; 1; 5; 10]
$p_{H_2O}$ (%)	[1; 10; 50; 90]
$P$ (%)	[45; 60; 80]
$q_{Sior}$	[0.31; 0.38; 0.47; 0.62]
$s$	[-3.5; -5]

**Table 5.** Six models best fitting the SED.

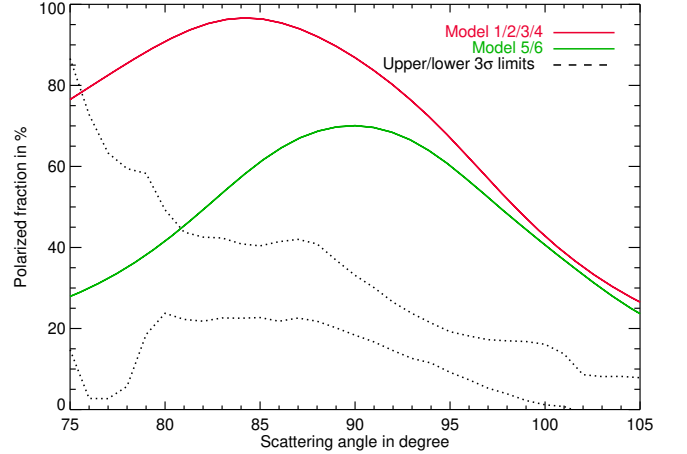
Model	Theory	$a_{min}$	$P$	$p_{H_2O}$	$q_{Sior}$	$s$	$\chi^2$
1	DHS	5	60%	1%	0.31	-3.5	3.0
2	DHS	5	60%	1%	0.31	-5.0	3.0
3	DHS	5	60%	1%	0.38	-5.0	3.4
4	DHS	5	60%	1%	0.38	-3.5	3.5
5	Mie	10	80%	1%	0.31	-5.0	3.7
6	Mie	10	80%	1%	0.31	-3.5	3.9

**Fig. 7.** SED of the best model compared to measurements.

(see Table 5) than the value  $q_{Sior} = 0.47$  set by Augereau et al. (1999).

### 5.3. Comparison with the polarimetric observables

In Fig. 8, we compared our measurements with the predicted polarized fraction for the six models presented in Table 5. The dust population that is compatible with the SED overpredicts the polarized fraction. Indeed, the large grains with  $a_{min} = 5\mu\text{m}$  or  $10\mu\text{m}$  that fit well the SED have high polarized fractions, es-

**Fig. 8.** Polarized fraction from the six models best fitting the SED. We overplotted the  $3\sigma$  common range between the NE and SW measurements.

pecially those whose properties were calculated using the DHS theory. If we relax the constraint on the SED, we can find models that predict a polarized fraction around 30% in the ansae with a  $\chi^2$  below 10, however, the peak polarized fraction occurs around  $90^\circ$ , as visible for the models 5 and 6 in Fig. 8, and this is incompatible with our measurements. As a matter of fact, all models that predict an increase in the polarized fraction greater than 3% between  $90^\circ$  and  $80^\circ$  have a very high polarized fraction above  $70^\circ$ .

### 5.4. Scattered light images

The best models fitting the SED are not compatible with our scattered light images. To illustrate this mismatch qualitatively, we show in Fig. 9 the polarized and intensity image at Ks of our best model. The forward-scattering side of the intensity image is much brighter than the other side, which is inconsistent with our measurements. The inconsistency between the SED and anisotropy of scattering is a known issue that may be related to our assumption of hard spheres, as already noticed for the disc of HD 181327 by Schneider et al. (2006) and Lebreton et al. (2012). Interestingly this anisotropy is less strong in the DHS models than in the Mie models, suggesting that irregular particles tend to have a less strong forward scattering behaviour than perfect spheres. This outcome should be emphasized because it points in the right direction of improved and more realistic dust scattering models.



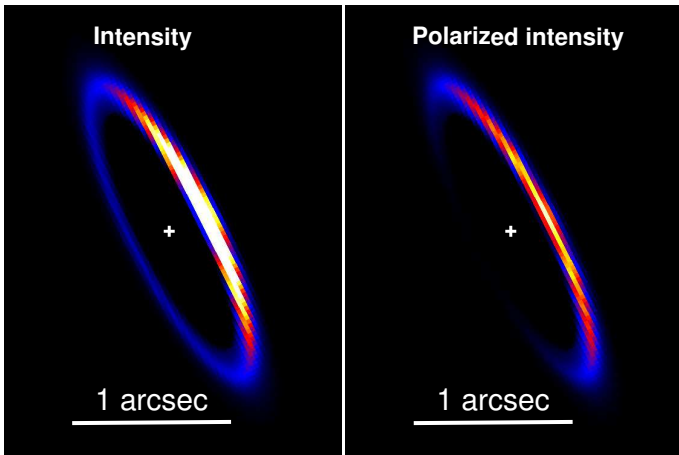


**Fig. 9.** Scattered light images in the Ks band from model 1 detailed in Table 5. The forward-scattering side is on the right. The color scale is linear is identical for the 2 images. Although the polarized intensity reproduces well the observations, a major discrepancy of all models concerns the intensity with a strong brightness asymmetry for the side inclined towards us.

**Table 6.** Comparison between the prediction of the six models best fitting the SED in the parameter space  $(a_{\min}, P, p_{H_2O}, q_{Sior}, s)$  explored and our measurements (in shaded grey) with respect to three observables. The uncertainty is given at a  $3\sigma$  level. We assumed for the models that the side inclined towards the Earth was the NW.

Model	Total disc flux density at Ks (mJy)	SE:NW ratio (Ks)	SE:NW ratio ( $L'$ )
Measurements	$3.7 \pm 0.26$	$1.1 \pm 0.3$	$0.9 \pm 0.18$
1	4.0	0.22	0.18
2	4.1	0.22	0.18
3	4.1	0.22	0.18
4	4.1	0.22	0.18
5	3.7	0.06	0.04
6	3.7	0.06	0.04

To provide a quantitative comparison with our measurements, we selected three relevant observables and compared them to the theoretical predictions. These three observables are shown in Table 6. The first one is the total disc flux at Ks that is compared to the extrapolated value from our HST re-reduced image. The last two are the brightness ratios at Ks and  $L'$  between the two sides of the disc inclined towards us and away from us (SE and NW sides). The area used to compute this ratio is an elliptical annulus of semi-major and semi-minor axis  $1.07''$  and  $0.27''$  and of width  $0.2''$ . For the aforementioned reasons, we only considered the regions in this annulus within  $40^\circ$  of the ansa. In Table 6, we compare these measurements to the predictions of our scattered light models. Overall, the total disc flux at Ks is well predicted by the six models. The main discrepancy comes from the brightness ratio between the forward and backward side of the disc : none of the six models have a SE side brighter than the NW and none of them can explain the inversion in brightness that seems to happen between the Ks and the  $L'$  filter. On the contrary, these models show that the brightness asymmetry gets stronger with increasing wavelengths.

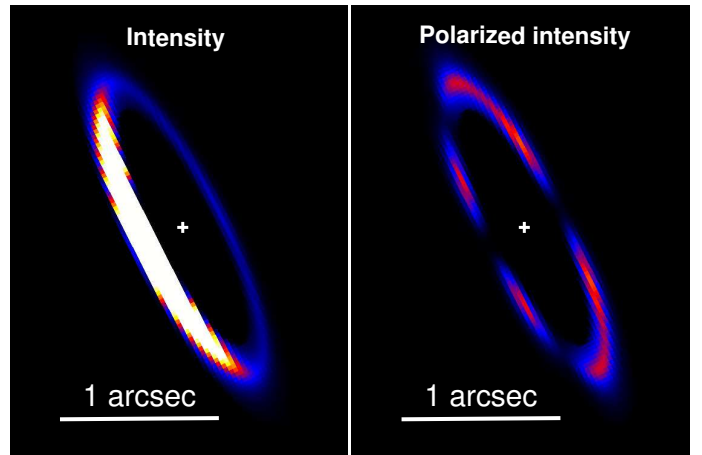


**Fig. 10.** Scattered light images in the Ks band from a model with  $(a_{\min}, P, p_{H_2O}, q_{Sior}, s) = (1, 80, 50, 0.62, -5)$ . The color scale is linear and the range is ten times larger for the intensity image than for the polarized image. The forward scattering side is on the left.

### 5.5. An incompatibility between the SED and the scattered light

So far, we demonstrated that the best models fitting the SED cannot explain the scattered light observations. Three basic features cannot be described by those models:

1. a change in the brightest side between polarized and unpolarized light,
2. a low anisotropy of scattering in unpolarized light, in other words, a SE:NW ratio close to 1 both at Ks and  $L'$ ,
3. a decrease in the anisotropy of scattering with increasing wavelength.

Based on a few examples taken from our grid of models, we will show that there are no solutions that can fully explain these features in our reasonably exhaustive exploration of the parameter space.

#### 5.5.1. Change in the brightest side between polarized and unpolarized light

In our baseline scenario, we cannot find any models where the brightest side changes between polarized and unpolarized light. Considering the alternative scenario, namely a SE forward-scattering-side, we could find such scattering behaviours among our grid of models when the properties are computed using the DHS theory. It happens for particles with a minimum size of  $1\mu\text{m}$  with a high water content of 50% to 90%. We provide an example of such a model in Fig. 10. There are however several caveats to these models:

1. they predict a polarized fraction in the ansa between 1% and 15%, which is too low to be compatible with our measurements,
2. they all provide a very strong asymmetry in unpolarized light, as visible in Fig. 10, with a high SE:NW brightness ratio above 10, which is not seen in our data.

Therefore the alternative scenario is even less compatible with the observables.

#### 5.5.2. Low anisotropy of scattering at Ks

The SE:NW brightness ratio of the six models that best fit the SED are very low (below 0.22), due to a very strong forward

scattering behaviour of micron-sized dust. This is inconsistent with our measured value of 1.1 at Ks. Even when considering all models in our parameter space, none achieves a SE:NW ratio greater than 0.4. Those models displaying ratios of 0.4 are found for large dust particles of minimum sizes  $10\mu\text{m}$  with a very high water content of 90%. They provide a high polarized fraction compatible with our data, but clearly fail to fit the SED in the far-infrared, with a  $\chi^2$  above 24.

### 5.5.3. Decrease in the anisotropy of scattering with wavelength

Among the solutions displayed in Table 6, none of them can explain the observed decrease in anisotropy of scattering with wavelength, illustrated in Fig. 5. The SE:NW brightness ratio is indeed further away from unity at  $L'$  than at Ks. Among the models able to explain that behaviour, their agreement with the SED is only marginal, with a  $\chi^2$  above 15 in all cases. Moreover, the anisotropy of scattering at  $L'$  is still strong with a SE:NW ratio below 0.5 in all cases, therefore they do not comply with our measured  $0.9 \pm 0.18$ .

## 6. Discussion

The most striking feature concerns the inconsistency between the NW/SE asymmetries in polarized and unpolarized light. We have shown that no matter what is assumed for the side of the disc inclined towards the Earth, no model compatible with the SED can fully explain the scattered light observations. We will now discuss the implications of each assumption regarding the forward-scattering side and propose future observations to answer this question.

### 6.1. Assumption 1: The NW side is inclined towards the Earth

This is the baseline scenario used in our grid of models and is illustrated in Fig. 9. In this context, the models that best fit the SED overpredict the polarized fraction as mentioned in section 5.3, but most importantly, none of them can explain the preferential backward scattering of the grains in unpolarized light. This case is very similar to that of the Fomalhaut debris disc, also inclined by about  $65^\circ$ . The bright side of the ring was shown to be inclined away from us through spectrally resolved interferometric observations (Le Bouquin et al. 2009). The best interpretation so far implies very large dust grains  $100\mu\text{m}$  whose diffraction peak is confined within a narrow range of scattering angles undetected from Earth given the system inclination (Min et al. 2012). In the case of HR 4796, this range of scattering angles could be as large as  $40^\circ$  since our constraints are very poor in this range in unpolarized light. In such conditions,  $30\mu\text{m}$  grains would be sufficient to explain the preferential back-scattering behaviour (cf Fig. 4 of Min et al. 2010), but this would be incompatible with the SED. Images at higher angular resolution are clearly required to validate this assumption. Their model does however not explore the wavelength dependence of the scattering phase function, which is required to explain the brightness inversion between the Ks and  $L'$  bands in unpolarized light.

### 6.2. Assumption 2: The NW side is inclined towards the Earth

Under this assumption, the disc is mainly forward-scattering up to  $2.2\mu\text{m}$  and the polarized image represents back-scattered light. This corresponds to the cases described in section 5.5.1. All our models are preferentially forward-scattering in unpolarized light, at all wavelengths between  $0.5$  and  $3.8\mu\text{m}$ , which represents a strong argument in favour of this hypothesis. However, this now contradicts the  $L'$  observations. Moreover, under this assumption, the SE:NW ratio would always be above 2.6 for all models, due to the strong forward-scattering predictions of the Mie and DHS theory, whereas our observations only show a value of  $1.1 \pm 0.3$ . The populations of grains with  $a_{\text{min}} = 1\mu\text{m}$ , large amount of water ice (above 30%) with scattering properties computed with the DHS theory could fit within this framework, as detailed in section 5.5.1. In this scenario, the offset of the disc detected along the minor axis both in the Ks polarized image and the  $L'$  unpolarized image, could slightly compensate this large asymmetry since the NW side would be closer to the star. Because the flux of the disc scattered light scales with the squared distance from the star, if we assume an offset of  $5.5\text{AU}$ , the NW side would only be 35% brighter, which is still not sufficient to reduce the SE:NW ratio to make it compatible with our measurement of  $1.1 \pm 0.3$ .

### 6.3. Validation of the optically thin hypothesis

All models presented here rely on the assumptions that the disc is optically thin. We validated this hypothesis by re-running the simulations of the best models with the correct disc mass necessary to fit the SED. Model 1 predicts a disc mass of  $0.2M_\oplus$  distributed among particles between  $5\mu\text{m}$  and  $10\text{mm}$ . The opacity reaches 0.08 perpendicular to the midplane of the disc and 0.8 along the mid-plane, which validates our hypothesis. We investigated on a few examples whether a more massive disc could explain the change in the brightest side with wavelength but could not find models compatible with our observations. An idea proposed to explain the spectral behaviour of the dust is indeed that the disc is optically thick in the optical and up to the Ks band and becomes optically thin in the  $L'$  band. However, we could not recreate this change in brightness. In particular, even for an optically thick disc, the brightest side remained the forward scattering side. We noticed from these models that the size of the ring should appear smaller for an optically thick disc, because most of the light is emitted by the inner regions of the ring. We do not notice such a change within error bars, though. This analysis goes beyond the initial scope of our paper and we leave the analysis of the transition between an optically thin and an optically thick disc to a further study.

### 6.4. Follow up observations

The questions raised by this new polarimetric view of the disc clearly call for further work on the observational and theoretical sides. A limitation of the current observations in unpolarized light is the inability to reveal the disc along the minor axis. This is however of great interest because the models predict the highest contrast between the forward and backward scattering side at this location. These observations are now possible with instruments such as SPHERE (Beuzit et al. 2008) or GPI (Macintosh et al. 2014), using reference star subtraction instead of ADI to avoid the problem of disc self-subtraction at such a short separation (Milli et al. 2012), thanks to the improved PSF

stability. With their polarimetric capabilities, a determination of the scattering phase function and polarized fraction at all angles scattered towards the Earth will be possible. With the near-infrared instrument SPHERE/IRDIS (Langlois et al. 2010), we can expect to reveal the spectral dependance of the phase matrix from the K band to the Y band, and maybe down to the V band with the visible instrument SPHERE/ZIMPOL (Schmid et al. 2010) with sufficient observing time. Such observations would be of great interest to compare the empirical phase functions and polarized fractions to that measured in laboratory on cosmic dust analogs (see for instance Volten et al. 2007). Resolved images of the thermal emission of the dust with the radiotelescope ALMA should provide additional constraints on the dust mass and thus the optical thickness of the disk in scattered light, as it was already done for Fomalhaut (Boley et al. 2012) and  $\beta$  Pictoris (Dent et al. 2014).

## 7. Conclusions

Our new observations show a clear detection of the polarized light of the debris disc surrounding HR 4796. Thanks to the PDI technique, the disc morphology can be probed more accurately at short separations, close to the minor axis. Starting from constraints on the dust grains based on previous modelling, we explored the compatibility of a grid of models with the scattered light both in intensity and polarization as predicted by two theories of light scattering: EMT-Mie and EMT-DHS. Our results confirm the earlier modelling suggesting that large grains are needed to explain the mid to far-infrared excess of the star. Both theories predict a strong forward/backward brightness asymmetry in polarized and unpolarized light, which is not consistent with the observational constraints showing that the SE side is brighter in unpolarized light from the visible up to  $2.2\mu\text{m}$ , whereas the NW side is brighter in polarization. We explore different scenarios to explain this apparent contradiction. Two conclusions emerge from this work. First, this shows that the dust particles are probably not spherical, as already pointed out by Debes et al. (2008) and Augereau et al. (1999). This is why the Mie theory and in a smaller extent the statistical approach of the DHS theory are probably inadapted to reproduce the scattering properties of these large and irregular fluffy aggregates. Even if not perfect, we note that the DHS theory is going in the right direction and provides a closer match to our observations than the Mie theory. Secondly, the case of HR 4796 is probably very similar to that of Fomalhaut where backward-scattering was already shown to challenge these traditional theories of scattering by spherical particles. A new generation of models is clearly needed, and observational constraints will come along to refine them. In the optical and near-infrared, high-resolution imagers such as GPI and SPHERE will be able to test whether a diffraction peak is observed for small scattering angles, as predicted by the Mie theory for circular grains, and will measure with high accuracy the phase function and polarized fraction over a much wider range of scattering angles and at various wavelengths.

*Acknowledgements.* J.M. acknowledges financial support from the ESO studentship program and the Labex OSUG2020. C. Pinte acknowledges funding from the Agence Nationale pour la Recherche (ANR) of France under contract ANR-2010-JCJC-0504-01. We would like to thank John Krist for his initial help with the NICMOS data and we thank ESO staff and technical operators at the Paranal Observatory.

## References

Augereau, J. C., Lagrange, A. M., Mouillet, D., Papaloizou, J. C. B., & Grorod,

- P. A. 1999, *A&A*, 348, 557  
 Avenhaus, H., Quanz, S. P., Schmid, H. M., et al. 2014, *ApJ*, 781, 87  
 Beuzit, J.-L., Feldt, M., Dohlen, K., et al. 2008, in *Society of Photo-Optical Instrumentation Engineers (SPIE) Conference Series*, Vol. 7014, *Society of Photo-Optical Instrumentation Engineers (SPIE) Conference Series*  
 Boley, A. C., Payne, M. J., Corder, S., et al. 2012, *ApJ*, 750, L21  
 Canovas, H., Rodenhuis, M., Jeffers, S. V., Min, M., & Keller, C. U. 2011, *A&A*, 531, A102  
 Debes, J. H., Weinberger, A. J., & Song, I. 2008, *ApJ*, 684, L41  
 Dent, W. R. F., Wyatt, M. C., Roberge, A., et al. 2014, *Science*, 343, 1490  
 Girard, J. H. V., Kasper, M., Quanz, S. P., et al. 2010, in *Society of Photo-Optical Instrumentation Engineers (SPIE) Conference Series*, Vol. 7736, *Society of Photo-Optical Instrumentation Engineers (SPIE) Conference Series*  
 Graham, J. R., Kalas, P. G., & Matthews, B. C. 2007, *ApJ*, 654, 595  
 Hinkley, S., Oppenheimer, B. R., Soummer, R., et al. 2009, *ApJ*, 701, 804  
 Jayawardhana, R., Fisher, R. S., Hartmann, L., et al. 1998, *ApJ*, 503, L79  
 Koerner, D. W., Ressler, M. E., Werner, M. W., & Backman, D. E. 1998, *ApJ*, 503, L83  
 Lagrange, A.-M., Boccaletti, A., Milli, J., et al. 2012a, *A&A*, 542, A40  
 Lagrange, A.-M., Milli, J., Boccaletti, A., et al. 2012b, *A&A*, 546, A38  
 Langlois, M., Dohlen, K., Augereau, J.-C., et al. 2010, in *Society of Photo-Optical Instrumentation Engineers (SPIE) Conference Series*, Vol. 7735, *Society of Photo-Optical Instrumentation Engineers (SPIE) Conference Series*  
 Le Bouquin, J.-B., Absil, O., Benisty, M., et al. 2009, *A&A*, 498, L41  
 Lebreton, J., Augereau, J.-C., Thi, W.-F., et al. 2012, *A&A*, 539, A17  
 Lenzen, R., Hartung, M., Brandner, W., et al. 2003, in *Society of Photo-Optical Instrumentation Engineers (SPIE) Conference Series*, Vol. 4841, *Instrument Design and Performance for Optical/Infrared Ground-based Telescopes*, ed. M. Iye & A. F. M. Moorwood, 944–952  
 Li, A. & Lunine, J. I. 2003, *ApJ*, 590, 368  
 Low, F. J., Smith, P. S., Werner, M., et al. 2005, *ApJ*, 631, 1170  
 Macintosh, B., Graham, J. R., Ingraham, P., et al. 2014, *ArXiv e-prints*  
 Mie, G. 1908, *Ann. Phys. Leipzig*, 25, 377  
 Milli, J., Lagrange, A.-M., Mawet, D., et al. 2014, *ArXiv e-prints*  
 Milli, J., Mouillet, D., Lagrange, A.-M., et al. 2012, *A&A*, 545, A111  
 Min, M., Canovas, H., Mulders, G. D., & Keller, C. U. 2012, *A&A*, 537, A75  
 Min, M., Hovenier, J. W., & de Koter, A. 2005, *A&A*, 432, 909  
 Min, M., Kama, M., Dominik, C., & Waters, L. B. F. M. 2010, *A&A*, 509, L6  
 Moerchen, M. M., Churcher, L. J., Telesco, C. M., et al. 2011, *A&A*, 526, A34  
 Mouillet, D., Lagrange, A.-M., Beuzit, J.-L., & Renaud, N. 1997, *A&A*, 324, 1083  
 Mulders, G. D., Min, M., Dominik, C., Debes, J. H., & Schneider, G. 2013, *A&A*, 549, A112  
 Nilsson, R., Liseau, R., Brandeker, A., et al. 2010, *A&A*, 518, A40  
 Pinte, C., Harries, T. J., Min, M., et al. 2009, *A&A*, 498, 967  
 Pinte, C., Ménard, F., Duchêne, G., & Bastien, P. 2006, *A&A*, 459, 797  
 Riviere-Marichalar, P., Pinte, C., Barrado, D., et al. 2013, *A&A*, 555, A67  
 Rousset, G., Lacombe, F., Puget, P., et al. 2003, in *Society of Photo-Optical Instrumentation Engineers (SPIE) Conference Series*, Vol. 4839, *Adaptive Optical System Technologies II*, ed. P. L. Wizinowich & D. Bonaccini, 140–149  
 Schmid, H. M., Beuzit, J. L., Mouillet, D., et al. 2010, in *In the Spirit of Lyot 2010*  
 Schneider, G., Silverstone, M. D., Hines, D. C., et al. 2006, *ApJ*, 650, 414  
 Schneider, G., Smith, B. A., Becklin, E. E., et al. 1999, *ApJ*, 513, L127  
 Schneider, G., Weinberger, A. J., Becklin, E. E., Debes, J. H., & Smith, B. A. 2009, *AJ*, 137, 53  
 Soummer, R., Perrin, M. D., Pueyo, L., et al. 2014, *ArXiv e-prints*  
 Soummer, R., Pueyo, L., & Larkin, J. 2012, *ApJ*, 755, L28  
 Stokes, G. G. 1852, *Royal Society of London Philosophical Transactions Series I*, 142, 463  
 Thalmann, C., Janson, M., Buenzli, E., et al. 2011, *ApJ*, 743, L6  
 Thébaud, P. 2009, *A&A*, 505, 1269  
 Tinbergen, J. 2005, *Astronomical Polarimetry*  
 Volten, H., Muñoz, O., Hovenier, J. W., et al. 2007, *A&A*, 470, 377  
 Voshchinnikov, N. V., Videen, G., & Henning, T. 2007, *Appl. Opt.*, 46, 4065  
 Wahhaj, Z., Koerner, D. W., Backman, D. E., et al. 2005, *ApJ*, 618, 385  
 Wahhaj, Z., Liu, M. C., Biller, B. A., et al. 2014, *ArXiv e-prints*  
 Witzel, G., Eckart, A., Buchholz, R. M., et al. 2011, *A&A*, 525, A130  
 Yamamura, I., Makiuti, S., Ikeda, N., et al. 2010, *VizieR Online Data Catalog*, 2298, 0